



## Article

# Modelling of Strain-Controlled Thermomechanical Fatigue Testing of Cast AlSi7Cu3.5Mg0.15 (Mn, Zr, V) Alloy for Different Aging Conditions

Pierre Heugue <sup>1</sup>, Daniel Larouche <sup>1,\*</sup>, Francis Breton <sup>2</sup>, Rémi Martinez <sup>3</sup>, X.-Grant Chen <sup>4</sup>  
and Denis Massinon <sup>5</sup>

- <sup>1</sup> Department of Mining, Metallurgy and Materials Engineering, Aluminum Research Center—REGAL, Laval University, 1065, Ave de la Médecine, Quebec, QC G1V 0A6, Canada; pierre.heugue@gmail.com
- <sup>2</sup> Rio Tinto, Arvida Research and Development Centre, 1955, Mellon Blvd, Saguenay, QC G7S 4K8, Canada; francis.breton@riotinto.com
- <sup>3</sup> Linamar Corporation—The Center, 700 Woodlawn Road West, Guelph, ON N1K 1G4, Canada; remi.martinez@linamar.com
- <sup>4</sup> Department of Applied Sciences, The University of Quebec at Chicoutimi, 555 Boul. de l'Université, Saguenay, QC G7H 2B1, Canada; xgrant\_chen@uqac.ca
- <sup>5</sup> Montupet, 3, Rue de Nogent, 60290 Laigneville, France; denis.massinon@gmail.com
- \* Correspondence: daniel.larouche@gmn.ulaval.ca; Tel.: +1-418-656-2153; Fax: +1-418-656-5343

**Abstract:** Thermomechanical fatigue loadings (TMF) applied on components in a certain temperature range with a variable state of stress (tensile and/or compression) produce a localized concentration of plastic strains that results in crack initiation and propagation. The time evolution of plastic strains must be known a priori to predict the lifetime of a part submitted to TMF loadings, which requires an extensive campaign of mechanical characterization conducted at different temperatures and aging conditions. Such a campaign was proposed for the aluminum alloy AlSi7Cu3.5Mg0.15 (Mn, Zr, V), which is recognized as being creep resistant. Combined isothermal low-cycle fatigue and isothermal creep tests were performed on this alloy to determine the constitutive parameters based on the Lemaitre and Chaboche (LM&C) viscoplastic model. These laws were implemented within the finite element simulation software (Z-set) to model the response of the alloy to a thermomechanical fatigue test. The results of TMF Z-Set simulations, using the LM&C model adapted for two aging conditions, were then compared with results obtained from “Out of Phase” thermomechanical fatigue testings (OP-TMF) performed on a Gleeble 3800 machine. The modelling of the OP-TMF test revealed the complexity of the mechanical behavior of the material induced by the temperature gradient prevailing along with the cylindrical specimen. It was found that a better prediction of the evolution of plastic strains requires taking into account a larger range of plastic strain rates conditions for the determination of the constitutive law and eventually includes the role of the microstructure in the evolution of the material behavior, starting first with the yield stress.

**Keywords:** 319 cast alloy; thermo-mechanical fatigue; Gleeble 3800 system; cyclic hardening



**Citation:** Heugue, P.; Larouche, D.; Breton, F.; Martinez, R.; Chen, X.-G.; Massinon, D. Modelling of Strain-Controlled Thermomechanical Fatigue Testing of Cast AlSi7Cu3.5Mg0.15 (Mn, Zr, V) Alloy for Different Aging Conditions. *Metals* **2022**, *12*, 1258. <https://doi.org/10.3390/met12081258>

Academic Editor: Andrey Pozdniakov

Received: 8 June 2022  
Accepted: 22 July 2022  
Published: 26 July 2022

**Publisher's Note:** MDPI stays neutral with regard to jurisdictional claims in published maps and institutional affiliations.



**Copyright:** © 2022 by the authors. Licensee MDPI, Basel, Switzerland. This article is an open access article distributed under the terms and conditions of the Creative Commons Attribution (CC BY) license (<https://creativecommons.org/licenses/by/4.0/>).

## 1. Introduction

### 1.1. Generalities on Thermomechanical Fatigue of Automotive Cylinder Head

The “downsizing” of the new generations of internal combustion engines helps to greatly limit polluting emissions by improving internal combustion, limiting friction and optimizing turbo-compression in order to provide significant specific power. Increasing the specific power of an engine could only be achieved by increasing the temperature and pressure, which generates high thermomechanical stresses in cylinder heads for instance. Thermal fatigue is caused by engine start and stop cycles and is considered as a low cycle load mode [1]. Mechanical fatigue is caused by pressure variation in the combustion chamber [2]. The three main factors significantly affecting the resistance to mechanical

fatigue are the design of the cylinder heads, the intrinsic fatigue resistance of the alloy (which is affected by the number of impurities or porosities) and the residual stresses induced by the heat treatment [3,4].

The critical areas for thermomechanical fatigue crack initiation are located near the thin walls and more particularly near the water pipes in the valve seat bridge (inter-valve bridge) of the automotive cylinder head. An internal combustion engine valve seat is the part on which the intake or exhaust valves come into contact to interact with the combustion chamber. Valve seats are critical areas of thermal engines. Indeed, if they are poorly positioned, oriented, cracked or poorly machined, leaks in the valves will occur, reducing the pressure in the cylinder and its lifetime. In addition, the valve seats are subject to significant thermal stresses, especially the exhaust valves which are not cooled by the fuel, and mechanical stresses due to high contact and abrasion pressures, essentially due to residues such as soot (Figure 1).

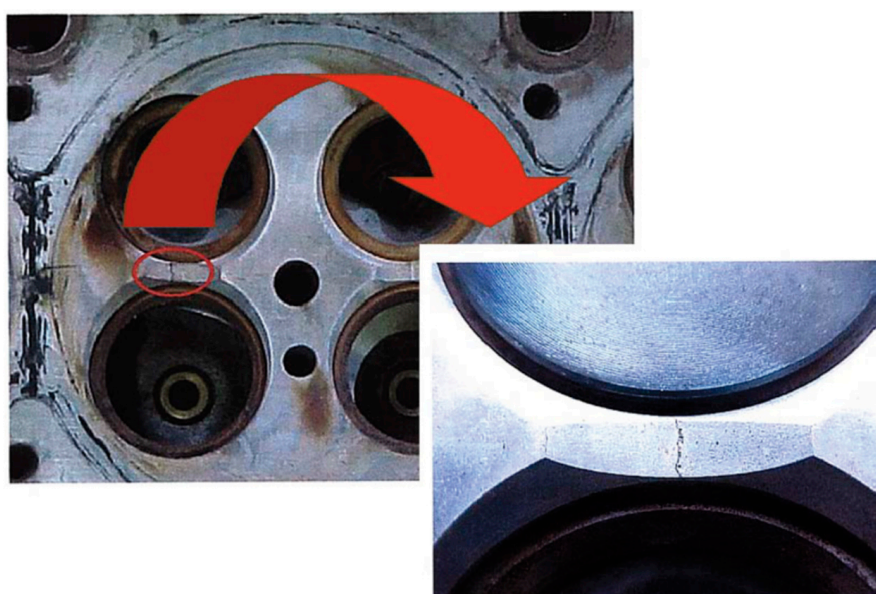


**Figure 1.** Initiation of crack on the bridge between the valve seats for an automotive cylinder head (©Montupet).

The cyclic stresses causing fatigue crack propagation at high temperatures do not necessarily result from the application of external physical loads. They can also be created by thermal strain. In thermomechanical conditions, the total strain ( $\varepsilon_{tot}$ ) is the sum of the thermal strain ( $\varepsilon_{th}$ ) and mechanical strain ( $\varepsilon_{mec}$ ); the latter includes the elastic ( $\varepsilon_{el}$ ) and inelastic ( $\varepsilon_{inel}$ ) strain component, so that:

$$\varepsilon_{tot}(t) = \varepsilon_{th}(t) + \varepsilon_{mec}(t) = \alpha(T) * (T(t) - T_0) + \varepsilon_{el}(t) + \varepsilon_{inel}(t) \quad (1)$$

where  $\alpha$  is the coefficient of linear thermal expansion,  $T_0$  is the reference temperature and  $T(t)$  is the test temperature.

In thermomechanical fatigue, the evolution of the thermal and mechanical strains can be in-phase or out-of-phase. Thus, two major tests are generally conducted in a TMF test: the in-phase cycle, where the stress and temperature increase and decrease simultaneously, and the antiphase cycle, where the stress increases while the temperature decreases and vice-versa. The most damaging loading conditions in engine components have been identified as being the out-of-phase thermomechanical fatigue (OP-TMF) [1,5,6].

The Gleeble<sup>®</sup> machine seems to be the best compromise for the implementation of TMF tests [7] because it involves joule heating in the test piece combined with airflow cooling. Unlike induction heating, which generates heat only in the subsurface periphery, the Gleeble<sup>®</sup> system produces heat in the entire volume, generating a small radial and axial

gradient on the length of the useful area of the sample. The major issue concerning this type of tests remains the proper continuous control and measurement of the temperature of the test specimen.

### 1.2. Thermomechanical Fatigue of Cast Aluminium Alloys

In the last ten years, the interest in the thermomechanical fatigue of precipitation-hardened aluminum alloys for mechanical applications has greatly increased. The first experimental work on the subject [8] was conducted to develop a constitutive model based on creep plasticity in the A319 T7 alloy. The results revealed that the stress–strain behavior was strongly influenced by the decomposition of metastable precipitates  $\theta'$  and the progressive coalescence of the  $\theta$  phase within the dendrites, which lead to softening. Subsequently, Toyoda et al. [9] reported a preferred orientation of the precipitates, parallel to the loading axis, during a TMF test on an Al-Si-Cu-Mg alloy between 50 °C and 250 °C under OP conditions. The observations made before and after the tests showed that the transformation of the phase  $\theta''$  into precipitates  $\theta'$ -Al<sub>2</sub>Cu caused the reduction in the stresses (softening). The authors explained it by a re-dissolution of the  $\theta''$  phase, followed by the formation and growth of  $\theta'$  by the Ostwald maturation. It has been shown that the precipitates which are oriented perpendicular to the loading axis are reduced in size, while the precipitates which are oriented parallel, grow. The mechanism of preferential orientation of the precipitate plates by stress aging [10,11] is due to a large crystal lattice mismatch in the direction perpendicular to the surface of the platelet precipitate. When subjected to compression perpendicular to the surface of the precipitate plates during aging, the crystalline mismatch is thermodynamically adjusted so that the overall strain energy of the matrix is reduced. Precipitates  $\theta'$  would preferentially align in a single direction due to the application of high-temperature compression stresses during OP TMF loading.

Jointly, many authors have examined the influence of fatigue with a large number of High Cycle Fatigue (HCF) cycles in thermomechanical (non-isothermal) behavior on AlSi6Cu4-T6/T7 [12], AlSi10Mg-T6 [13] and AlSi7Mg-T6 [13,14] alloys between 50 °C and 300 °C. Early observations showed a decrease in compressive stress caused by dynamic relaxation and temperature-dependent creep effects. In addition, over-aging during the TMF test of AlSi7Mg-T6 [14] caused by the coalescence of Mg<sub>2</sub>Si precipitates above a threshold temperature of 250 °C, greatly reduced its fatigue life. Azadi et al. [15] studied the influence of the T6 heat treatment of an A356 compared to an untreated state for OP-TMF testing and they showed that plastic strain increases severely during the fatigue lifetime of T6 heat-treated alloy due to the over-aging phenomenon.

More recently, the work of Grieb [5] focused on the TMF life expectancy of several alloys (AlSi7Mg-T6, AlSi5Cu1-T6, AlSi5Cu3-T7, AlMg3Si1-T6, AlMg3Si1 (Cu)-T6 and AlMg3Si1 (Sc, Zr)-T5) for the inter-valve bridge of a cylinder head. Two damage models were used (the Chaboche model and a damage prediction model developed by the IWM Fraunhofer Institute, Freiburg GE) on a realistic geometry of the inter-valve bridge to reproduce the behavior of a real cylinder head. The tests were conducted in a range from 50 °C to 400 °C. The type of material model used in these studies, however, was not specified. Predictions of the fatigue life of the specimens were obtained using the finite element analysis (FEA) results and compared with the experimental results for the fatigue strength of the actual specimens. This study was completed by the work of Delprete et al. [16] for a multiaxial approach.

In the same way, Toda et al. [17] modeled the TMF behavior of an AlSi7Mg0.3 alloy using a multistep numerical simulation. The material behavior was calculated based on a dual-phase model, in which the eutectic microconstituent was assumed to have the stress–strain relationship that was previously calculated based on a single particle model. These works, as well as those of Merhy et al. [18], emphasized the appearance of cracks at the interface between the Si particles and the  $\alpha$ -Al matrix. It has been observed that cracks are propagated along slip bands in the  $\alpha$ -Al matrix and also along the constituent eutectic region due to poor thermomechanical misfit between the brittle phases and the matrix.

For an AlSi7Mg0.3Cu0.2-T6 alloy, Tsuyoshi et al. [19] were interested in the influence of the evolution of the precipitation during the OP-TMF tests at different times of aging at 250 °C (up to 100 h) and its effect on the fatigue life. They showed that the longer the time of aging, the longer the fatigue life was because it leads to the lower increment of the density of both dislocation and precipitates. For a hypereutectic Al-Si alloy, Wang et al. [20] have characterized the behavior of IP-TMF in order to evaluate the fatigue life for engine piston applications.

Finally, very recently, Huter et al. [1] have characterized the influence of Si and Cu on the anti-phase thermomechanical fatigue behavior of alloys AlSi6Cu4 (Sr), AlSi8Cu3 (Sr), AlSi7MgCu (Sr), AlSi7Mg (Sr) and AlSi10Mg (Sr), the latter in T79 or T74 conditions. It emerges that these elements play a major role in TMF lifespan mainly through particle interactions. Kliemt et al. [21] model TMF tests on an AlSi6Cu4 alloy using an FE simulation model. They were the first to use the Lemaître and Chaboche constitutive behavior laws for that purpose.

### 1.3. Thermoelectric Modelling of Joule Heating

In the context of a thermomechanical test, the temperature control of the specimen is a real challenge. The length of the hot zone of a Joule-heated specimen is determined from the measurement of the temperature profile [22,23] measured along with the test specimen, mainly with the use of welded or surface-bonded thermocouples. However, these tend to go off the hook making it difficult to instantly control the temperature. Han et al. [24] developed a technique to control the temperature of the hot zone without having to attach thermocouples to the specimen. This was performed with calibration curves giving the temperature of the hot zone of the specimen from the temperature of a point located outside of it which can, subsequently, be extrapolated for areas of very high temperatures [25].

Given the experimental difficulties in measuring the temperature of the hot zone, numerical simulation is an interesting alternative. It was initially implemented in the work of Zhan et al. [26] for the study of the thermal profile in steel specimens. Palama Bongo et al. [27] considered steel jaws to model the Joule heating and the determination of the hot zone in a specimen of A356 alloy. These two numerical approaches were only performed on a local assembly of the Gleeble<sup>®</sup> fixture (specimen and jaw only). On the Gleeble<sup>®</sup>, the temperature reading along the specimen indicates a parabolic thermal profile during Joule heating. Asymmetry may be observed on the thermal profile when unequal tightening torques are applied to the ends of the test piece on the jaws, which creates, between the mobile end and the fixed end of the Gleeble<sup>®</sup>, a difference in electrical contact resistance and thermal conductance [28].

## 2. Experimental

### 2.1. Samples Preparation

All cylindrical AlSi7Cu3.5Mg0.15 (Mn, Zr, V) samples ( $\phi$ 20.5 mm, length 200 mm) have been cast in the R&D center of Montupet (Laigneville, France) by gravity die casting technique in thermo-regulated metallic molds according to AFNOR standard (NF A57-702-1981) with Sr modification beforehand. A cast checking and quality monitoring (solidified alloy density, chemical composition controls and repetitive degassing of the melting bath every ten castings) have been performed for the entire production. Casting parameters have been calibrated to obtain samples with SDAS between 15 and 25  $\mu$ m (Figure 2). Each sample has been cast at the same liquid metal temperature,  $T_{\text{Ladle}} = 709 \text{ }^\circ\text{C} \pm 6 \text{ }^\circ\text{C}$ , in a mold controlled at a temperature  $T_{\text{Die}} = 149 \text{ }^\circ\text{C} \pm 6 \text{ }^\circ\text{C}$ . The chemical composition of alloy was analyzed by inductively coupled plasma-atomic emission spectroscopy (ICP-AES) using the IRIS Intrepid analyzer of Thermo Scientific, Waltham, MA, USA. Table 1 presents the general chemical composition obtained. All samples were submitted to a T7 heat treatment consisting first of a solution heat treatment (SHT) performed at 505 °C for 4 h with a heating rate of 8.5 K/min, followed by a cold-water quench to obtain the maximum solute saturation. Artificial aging was thereafter performed at 200 °C for 5 h. A

subset of the heat-treated samples, called hereafter T7S, was submitted to a soaking heat treatment. These samples were then overaged at 300 °C during 100 h to obtain a stabilized microstructure.

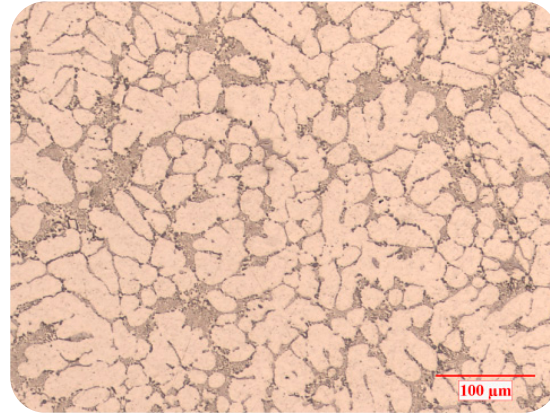


**Figure 2.** As-cast dendritic microstructure of the AlSi7Cu3.5Mg0.15 (Mn, Zr, V) alloy.

**Table 1.** General chemical composition of cast alloy from cast ingots.

AlSi7Cu3.5Mg0.15 (Mn, Zr, V)	Elements	Si	Cu	Mg	Fe	Ti	Mn	Zr	V	Sr	Zn
	% wt.	6.86	3.41	0.14	0.12	0.11	0.15	0.12	0.11	0.013	0.014

## 2.2. Characterization Methods

### 2.2.1. AlSi7Cu3.5Mg0.15 (Mn, Zr, V) As-Cast and As-Quenched Characterization

Cast alloy samples have been characterized through their metallurgical condition: as-cast and as-quenched. Samples for microstructural examination were sectioned from the cast cylinder, mounted, ground and polished using standard procedure. The polished sections were then examined with an optical microscope (ZEISS, Oberkochen, GE) and with electron probe microanalysis (EPMA-CAMECA SX100 with W filament, CAMECA, Gennevilliers, FRA) equipped with a wavelength dispersive spectrometer (WDS).

### 2.2.2. Isothermal Low Cycle Fatigue (LCF) and Creep Tests

In order to understand and characterize the effect of the different aging conditions on the mechanical behavior, isothermal LCF and creep tests were performed for the determination of the set of parameters included in the elastoviscoplastic model.

The LCF tests were performed under the strain control mode, applying a triangular signal with strain rates of  $10^{-3} \text{ s}^{-1}$ , a with strain and a mechanical strain amplitude of 0.5%. The creep test parameters are given in Table 2. The strain rate obtained during the secondary creep stage ranged from  $1.5 \times 10^{-9} \text{ s}^{-1}$  up to  $8.0 \times 10^{-7} \text{ s}^{-1}$ . A technical drawing of the specimen is given in Figure 3 for the LCF and creep specimens as per ASTM E606/E606M and ASTM E139-06, respectively.

The identification of parameters was done by graphical correlation between experimental and numerical integration on one Gauss point in Z-set. The elastoviscoplastic model [29,30] used is an extension of a classic viscoplasticity model with nonlinear kinematic and isotropic strain hardenings relevant for the representation of cyclic loadings. In this context, the Lemaître and Chaboche (LM&C) [31], model law for uni-axial loading was used and can be written as:

$$\sigma_{vp} = \sigma_y + K(|\dot{\epsilon}_p|)^{1/n} + Q\left(1 - e^{-b \cdot \epsilon_p}\right) + \frac{C_1}{D_1}\left(1 - e^{-D_1 \cdot \epsilon_p}\right) + \frac{C_2}{D_2}\left(1 - e^{-D_2 \cdot \epsilon_p}\right) \quad (2)$$

where  $\sigma_{vp}$  is the viscoplastic stress,  $\epsilon_p$  is the plastic strain,  $\dot{\epsilon}_p$  the plastic strain rate,  $\sigma_y$  is the yield strength of the undeformed material and  $C_1$ ,  $C_2$ ,  $D_1$  and  $D_2$  are the parameters

of the double kinematic strain hardening, with  $Q$  a constant giving the asymptotic value of the isotropic strain hardening corresponding to the stabilized cyclic regime and with  $K$  and  $n$  the coefficients of the Norton viscosity equation. The law has been split into two constitutive blocks (potentials): the first is based on an elastoviscosity (EV) potential and the second is based on an elastoplasticity (EP) potential. The EV block included a Norton equation with a zero-yield strength to relate with the creep results. The EP block included the yield strength plus the isotropic and kinetic hardening parameters to relate with the time-independent plasticity flow type. The combination of the two blocks was used for parameter identification according to the LCF hysteresis loops.

**Table 2.** Creep test parameters for LM&C identification.

Metallurgical Condition	Test T °C	Applied Stress (MPa)
<b><i>T7</i></b> S 505 °C during 4 h Water quench (20 °C) Aging 200 °C during 5 h	200	138
		148
		158
	300	50
		55
		60
<b><i>T7S</i></b> S 505 °C during 4 h Water quench (20 °C) Aging 200 °C during 5 h Holding at 300 °C during 100 h	200	108
		118.5
		138
	300	50
		55
		60

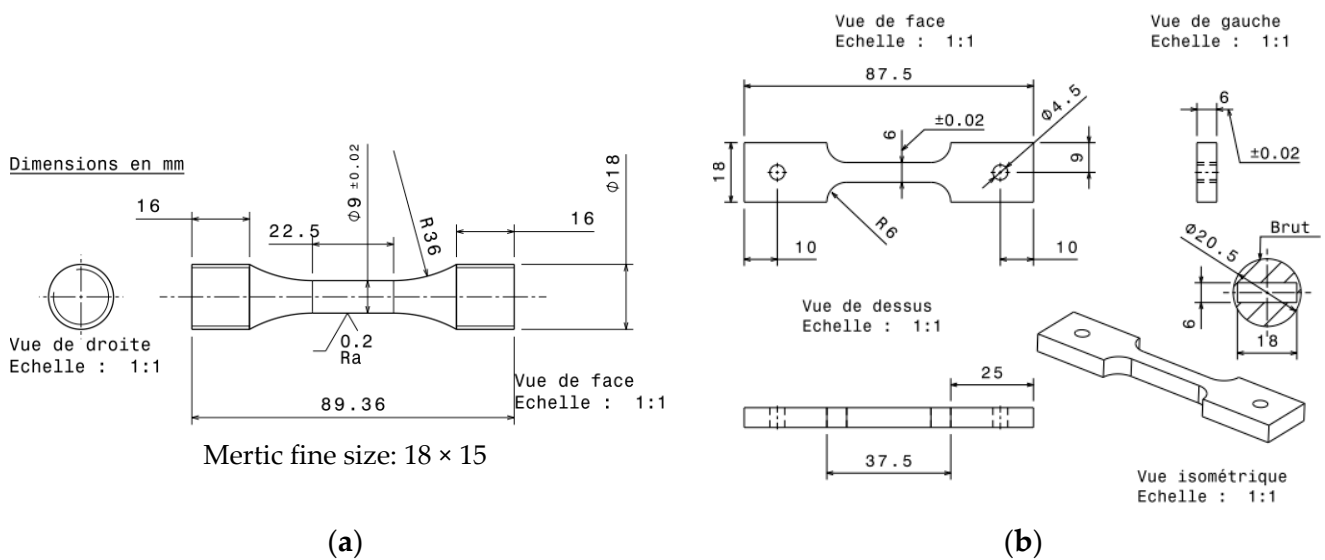


**Figure 3.** Technical drawing for (a) LCF samples and (b) creep samples (in mm).

### 2.2.3. Thermomechanical Fatigue Tests

OP-TMF tests were conducted on Gleeble<sup>®</sup> 3800 (Dynamic System Inc., Poestenkill, NY, USA) according to the procedure described in [7]. The strain was controlled with an extensometer having a gauge length of 25 mm located at the center of the specimen. The strain amplitude was adjusted in order to have a mechanical strain variation in the range  $\pm 0.5\%$  as the temperature at the center of the specimen varied between 60 °C and 300 °C. A technical drawing of the specimen is given in Figure 4, based on ISO 12111: 2011 and ASTM E2368-10.

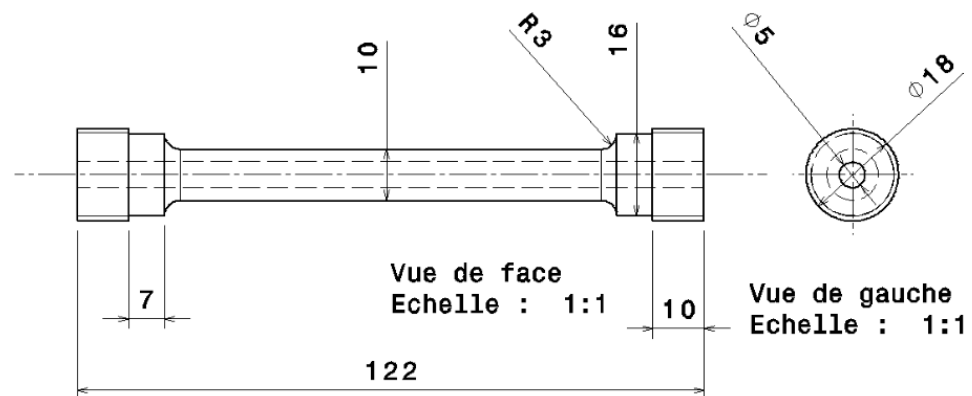


**Figure 4.** Technical drawing of TMF samples (size in mm).

#### 2.2.4. Comsol Thermoelectric Modelling

Comsol Multiphysics v5.3a has been used for the modelling of heat generated by the Joule effect and the heat transfer driven by the cooling system of the Gleeble<sup>®</sup>. The latter included water cooling of the grips and air cooling by forced convection inside the tube. The model included the sample attachment systems (jaws, grips, nuts and clips) to mimic as close as possible the real conditions. The objective of the modelling was to determine the evolution of the heat flows within the test piece during the heating and cooling phases of the TMF test between 60 °C and 300 °C, in order to implement them within the reduced mesh in Z-set for thermomechanical modelling. The material properties, boundary conditions and the calculation parameters are described in Appendices A and B.

#### 2.2.5. Z-Set Thermomechanical Modelling

The Z-set model was a 2D axisymmetric tubular sample. The external heat flux, the volumetric heat generated and the temperature profile obtained with the COMSOL simulation (Comsol Multiphysics v5.3a) were used and adapted to set the boundary conditions and the volumetric heat generated in the thermal simulation on Z-set. The calculations were made for the entire duration of the thermomechanical modelling, so a direct transfer of temperature distribution versus time could be made for the entire domain. The material properties used in the Z-set models were similar to those used in the COMSOL simulation. The constitutive parameters of the material were those optimized using the 2-potentials LM&C law. The coefficient of thermal expansion was calculated based on the volumetric mass (density) variation with temperature. All boundary conditions and the calculation parameters are described in Appendices A and B.

### 3. Results

#### 3.1. Metallurgical Characterization

Cast AlSi7Cu3.5Mg0.15 (Mn, Zr, V) samples present millimetric grain size and a measured secondary dendrite arm spacing (SDAS) of  $17.6 \pm 3.2 \mu\text{m}$ . Microstructures show very low porosity but many intermetallics that have been identified based on the literature [32], thermodynamic computations and the as-cast microprobe mapping analysis. Intermetallics like  $\alpha\text{-Al(Fe, Cu, Mn)Si}$ ,  $\beta\text{-AlFeSi}$ ,  $\text{Al}_2\text{Cu}$ ,  $\text{Al}_7\text{Cu}_2\text{Fe}$ ,  $\text{Al}_3$  (Zr, Ti, V) and  $\text{Al}_2\text{Si}_2(\text{Sr})$  intermetallic phases have been identified.

Phases remaining after SHT were according to the equilibrium calculation performed with Thermo-Calc at 505 °C with the TTAL7 database (Thermo-Calc Software, Solna, Stockholm, SE). The microstructure contained undissolved phases like  $\alpha\text{-Al(Fe, Cu, Mn)Si}$ ,  $\text{Al}_2\text{Si}_2(\text{Sr})$  intermetallics and the remaining  $\text{Al}_3(\text{Zr, V, Ti})$  dispersoids. The chemical composition in the dendrites was found uniform after the SHT, as this was confirmed by linear-scanning EPMA especially for Si and Cu contents at, respectively, about 1.0%wt. and 2.8%wt. More details on the as-quenched and T7 microstructure are given in [33].

### 3.2. LM&C Behavior Law from Isothermal LCF and Creep Testing

The LM&C parameters have been determined for the T7 and T7S conditions by graphical correlation with experimental isothermal LCF stress–strain hysteresis loops (Figure 5), except for the elastoviscous parameters, ( $K$  and  $n$ ), which were determined from the creep tests. The parameters were validated for various cycles up to 200 cycles for the T7 condition at 20 and 200 °C and, respectively, up to 350 and 1000 cycles for the T7S condition at 20 and 300 °C. The LM&C parameters for the AlSi7Cu3.5Mg0.15 (Mn, Zr, V) alloy are summarized in Tables 3 and 4. The closest LCF test condition associated with the TMF T7 condition was the one aged at 200°C for 24h and characterized at 200 °C and at room temperature.

The data at 300 °C were obtained by linearization of the experimental values at 20 °C and 200 °C, except for the yield strength and Young’s modulus, for which reasonable values were chosen.

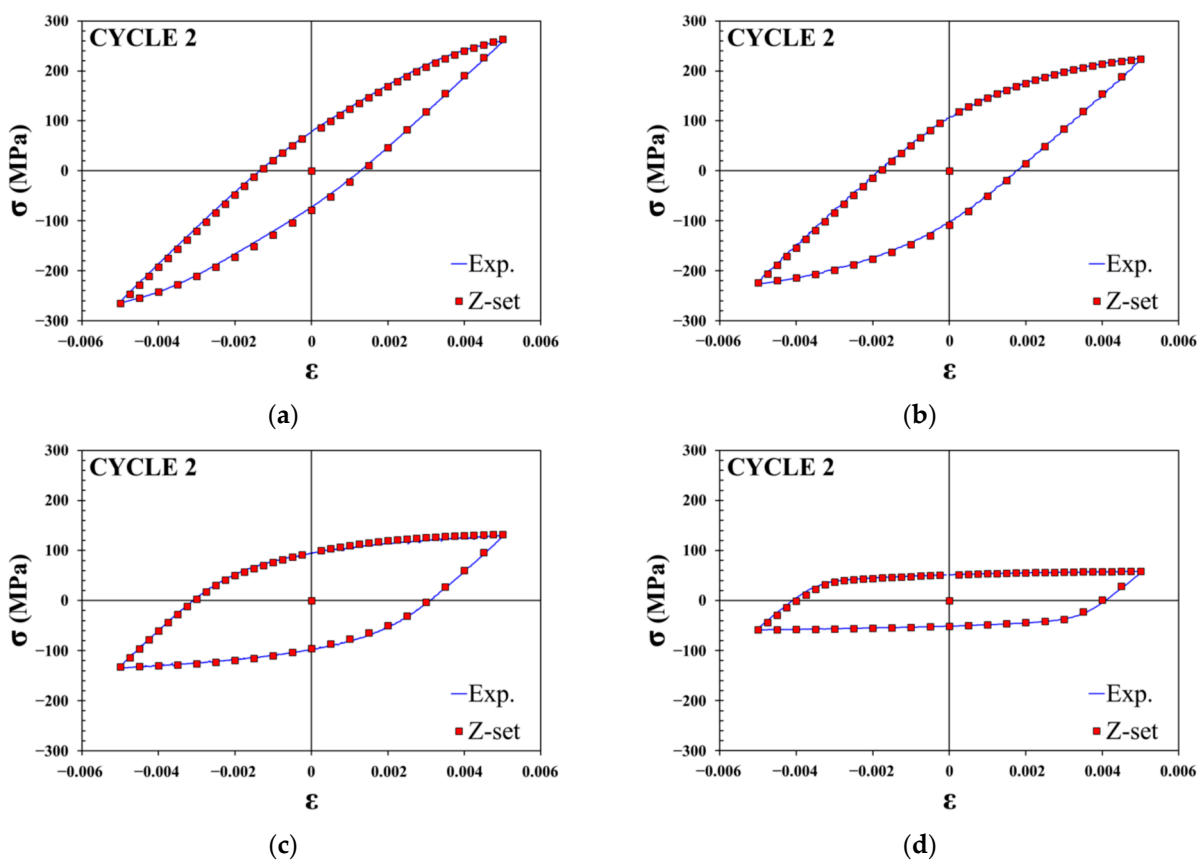


**Figure 5.** Cycle 2 of LCF strain–stress hysteresis loops with associated Z-set simulation for (a) T7 condition at room temperature, (b) T7 condition at 200 °C, (c) T7S condition at room temperature, and (d) T7S condition at 300 °C.

**Table 3.** Elastic and LM&C parameters used for modelling the mechanical behavior of AlSi7Cu3.5Mg0.15 (Mn, Zr, V) in the T7 condition.

Temperature (°C)	Isotropic Elastic ( $\nu = 0.3$ ) $E$ (MPa)	Block 1—EV ( $\sigma_y = 0$ )			Block 2—EP					
		$n$	$K$ (MPa·s <sup>1/n</sup> )	$C_1$ (MPa)	$D_1$	$C_2$ (MPa)	$D_2$	$\sigma_y$ (MPa)	$Q$	$b$
20	72,200	20.00	500.00	280,000	17,000	120,000	850	130	−15	1.5
200	69,904	13.74	536.91	542,500	10,190	50,500	650	107.5	−80	0.5
300	55,000	10.26	557.42	688,333	6406	11,889	567	40	−116	0.15



**Table 4.** Elastic and LM&C parameters used for modelling the mechanical behavior of AlSi7Cu3.5Mg0.15 (Mn, Zr, V) in the T7S condition.

Temperature (°C)	Isotropic Elastic ( $\nu = 0.3$ ) $E$ (MPa)	Block 1—EV ( $\sigma_y = 0$ )		Block 2—EP						
		$n$	$K$ (MPa·s <sup>1/n</sup> )	$C_1$ (MPa)	$D_1$	$C_2$ (MPa)	$D_2$	$\sigma_y$ (MPa)	$Q$	$b$
20	72,200	20.00	500.00	420,000	9100	31,000	550	33	5	0.55
300	58,119	3.3	19,173.83	225,000	9000	4000	300	22.5	−12.5	0.15

### 3.3. Thermoelectric Model

The simulation of three thermal cycles was performed with COMSOL to obtain a quasi-stabilized thermal profile in the model. The input parameters were selected in order to match the command linear variation of temperature between 60 and 300 °C at the surface of the tubular specimen (mid-position) for a cycle period of 100 s. Conductive heat flux and heat generated per unit volume by the Joule effect were calculated and implemented into the reduced mesh of the Z-set model to obtain the corresponding thermal profile. Figure 6a shows the calculated variation in temperature on the outer surface of the specimen for the points from 0 mm (middle) to 40 mm (end of the jaw) based on the Z-set thermal results. Figure 6b shows the temperature profile obtained at the peak of a cycle. These results were compared with those obtained experimentally by Qin et al. [7] under the same conditions of testing. The temperatures were measured with thermocouples welded along the outer surface of the specimen. It is thus possible to notice a fairly good agreement between the experimental points and the Z-set simulation result, according to the Comsol simulation.

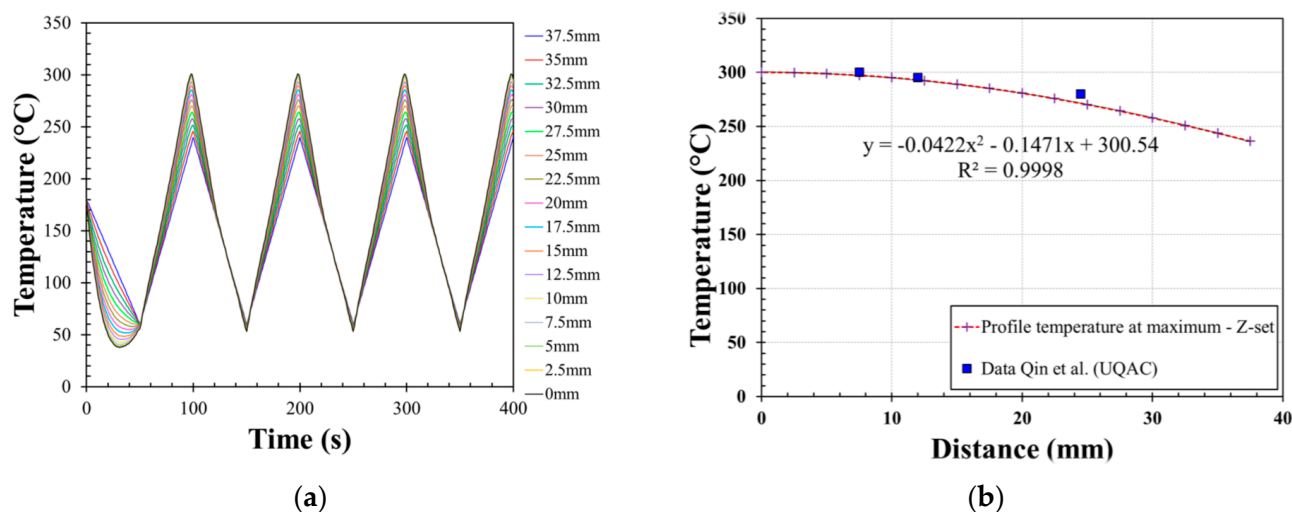


**Figure 6.** (a) Evolution of the surface temperature along the longitudinal axis of the specimen as modeled by Z-set, (b) profile temperature at the top of a cycle and comparison with experimental points on Gleeble®.

### 3.4. Thermomechanical Model

In order to faithfully reproduce the methodology used to perform a TMF test on Gleeble®, a PID controller has been integrated into the mechanical resolution program in Z-set. In fact, the TMF tests are carried out in strain control (for example  $\pm 0.5\%$  of  $\epsilon_{\text{mech}}$ ) at the level of the extensometer, thus in displacement with respect to the length between the knives of the extensometer, and it is therefore with the hydraulic cylinder of the movable jaw to associate the displacement of the device as a result of the strain instruction. At the output, the load cell measures the stress obtained for a given displacement. This is why, in the considered model, a setpoint value for displacement was imposed on a node close to the position of one of the knives of the experimental extensometer, respectively, at the

nodes at 11.75 mm and 10.75 mm of the low edge for the experimental test conditions T7 and T7S. The software is therefore compelled to respect this instruction by moving the “top” nodes so that the displacement of the imposed node scrupulously corresponds to that obtained experimentally by the extensometer. Thus, the displacement imposed for the T7 sample at the 11.75 mm node relative to the experimental total strain varies triangularly between  $[-0.019152 \text{ mm}$  and  $0.0316075 \text{ mm}]$  and for the T7S sample at the 10.75 mm node between  $[-0.0142975 \text{ mm}$  and  $0.0301 \text{ mm}]$ . In order to limit the mesh distortion caused by the fact that the mesh is stretching as the TMF test is extended, a non-displacement border condition on the radial axis has been imposed on the intersection node of the top (end of sample) and exterior edges. In addition, the bottom edge (middle of the sample) was imposed motionless along the longitudinal axis.

The results of stress hysteresis loops as a function of mechanical strain on cycle 2 are given in Figure 7 for conditions T7 and T7S. These loops are compared with experimental ones established under the same conditions on Gleeble<sup>®</sup>. The correlation between the experimental and the simulation is optimal for the T7S condition. On the other hand, condition T7 does not seem to present a suitable correspondence between the two curves. The simulation seems to overestimate the amplitudes of stresses and presents a too small  $\Delta\varepsilon_p$ .

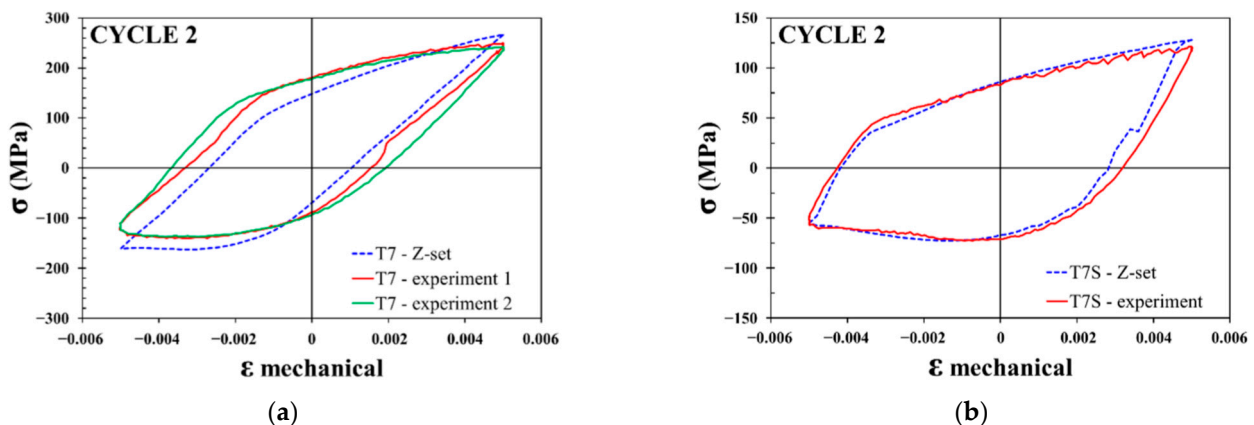


**Figure 7.** Hysteresis loops of mechanical strain-stress obtained by LM&C EV EP under condition  $\pm 0.5\%$  of  $\varepsilon_{\text{mech}}$  (a) T7, and (b) T7S compared to experimental test.

The evolution of the stress amplitude as a function of the number of cycles is presented in Figure 8. Here again, a very close fit is obtained for the T7S condition, while the results for the T7 condition show more deviation. In this case, the simulation predicts that hardening increases with time, but a clear softening effect was observed in the experiment. This highlights the fact that the modelling of the T7 condition requires taking into account the effect induced by the aging on mechanical behavior [34]. This can be achieved by integrating within the parameters a new evaluation of the  $\sigma_y$  based on the growth and dissolution of precipitates as a function of temperature and time. It would then be possible to reproduce the softening expected by stress aging in the first 100 cycles. This effect can be explained by Ostwald-ripening and the reorganization of the orientation of the  $\theta'$ -Al<sub>2</sub>Cu precipitates in the direction of the imposed mechanical strain, as discussed in [9].

Figure 9 shows the evolution of the stroke of the hydraulic cylinder of the mobile jaw during a Gleeble<sup>®</sup> OP-TMF test, which is compared to the displacement of the outer node at the upper end of the mesh (intersection between the top and the external edges) for the two metallurgical conditions. The simulated slope is higher than the slope observed in the T7 and T7S conditions by a factor 40 and 4.5, respectively. There is a factor 3 between the simulated slopes for T7S and T7, whereas this factor is around 27 for the experimental ones. It is important to notice that the difference of the displacement amplitudes on the cycles between experimental and simulation (Figure 9) is due to the fact that hydraulic cylinder of the movable jaw must catch up the mechanical backlash present on the whole system contrary to the results on the node of the sample geometrical mesh for the simulation.

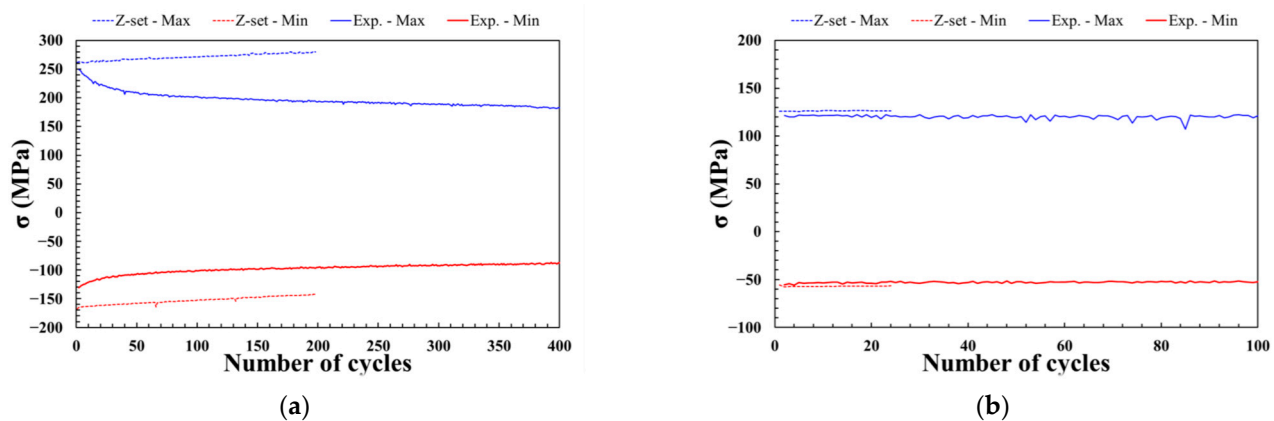


**Figure 8.** Stress amplitudes according to the number of cycles obtained with LM&C EV EP behavior law in (a) T7, and (b) T7S conditions by comparison with experimental tests.

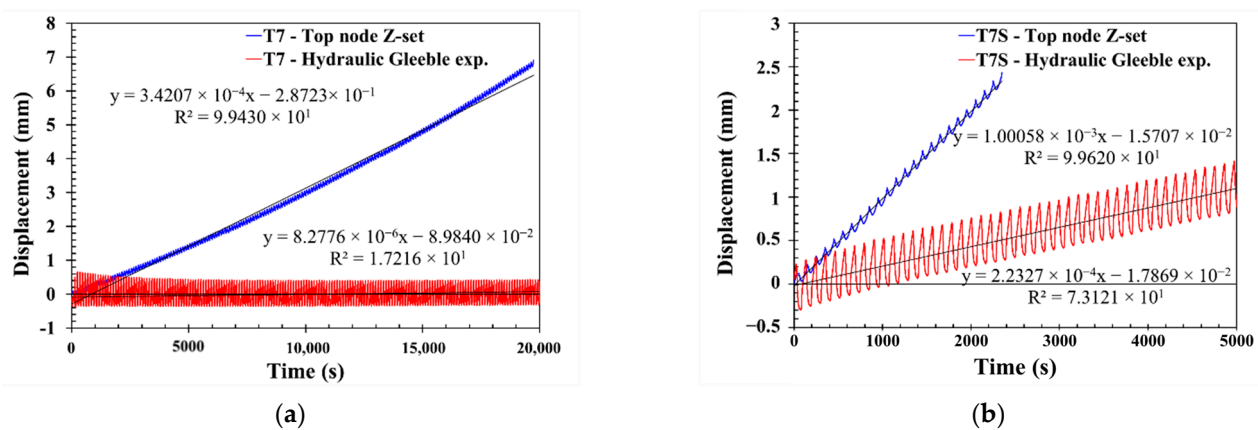


**Figure 9.** Experimental stroke of hydraulic cylinder for the movable jaw compared to the displacement of outside node at the upper end of the specimen (intersection of Top and Ext edges) to condition (a) T7 and (b) T7S calculated by the LM&C EV EP law.

#### 4. Discussion

The microstructures obtained with the T7 and T7S heat treatment present, respectively, fully-transformed  $\theta'$ -Al<sub>2</sub>Cu and  $\theta$ -Al<sub>2</sub>Cu precipitates according to a previous study made on the precipitation kinetics on this alloy [33]. This can be visualized with the time-temperature-transformation (TTT) diagram of this alloy, which is presented in Figure 10. This means that during an OP-TMF test reaching 300 °C, the alloy in T7 condition is subjected to microstructure evolution including stress aging with dissolution and reorientation of  $\theta'$ -Al<sub>2</sub>Cu precipitates and growth of  $\theta$ -Al<sub>2</sub>Cu. The alloy in T7S condition is however fully stabilized and softening of the material due to microstructure evolution is not expected.

As shown in the results section, the experimental and simulated TMF hysteresis loops are very similar for the T7S stabilized condition. They differ more significantly in the non-stabilized state (T7), suggesting that the evolution of the microstructure plays an important role in the evolution of hysteresis loops. This highlights the importance of using microstructure dependent material properties to mimic correctly the behavior of non-stabilized alloys.

Another interesting observation that has been made on samples tested with the Gleeble<sup>®</sup> device is the stretch occurring during the OP-TMF test, the latter being more or less significant depending on whether the microstructure was stabilized (T7S) or not (T7). In the stabilized state, the stretching (displacement of the movable jaw) was up to 8 mm, whereas it was only a fraction of a millimeter in the T7 condition (Figure 11). This behavior was reproduced by the Z-set simulation. However, the predicted displacements

are much larger in both cases (at least 30–40 times more for the T7 condition and at least 4–5 times more for the T7S condition). The cause of the difference between the simulated and experimental stretching effect is the temperature-dependent viscoplastic deformation of the material, which is experienced differently in the specimen because of the thermal gradient existing during the test. The agreement is qualitative in this case, but the desire to obtain a quantitative agreement, considering that the loops of hysteresis of the T7S state are really almost the same, pushed the understanding of the phenomena brought into play.

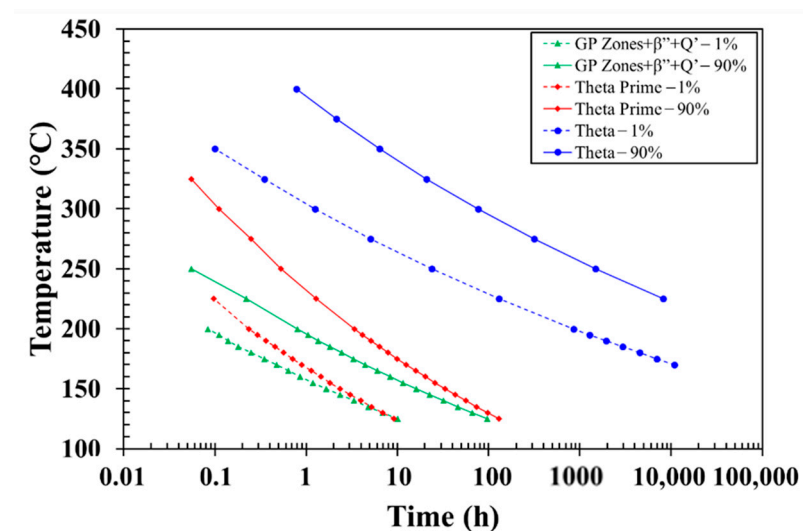


Figure 10. TTT diagram for precipitation in AlSi7Cu3.5Mg0.15 (Mn, Zr, V) alloy according to [33].

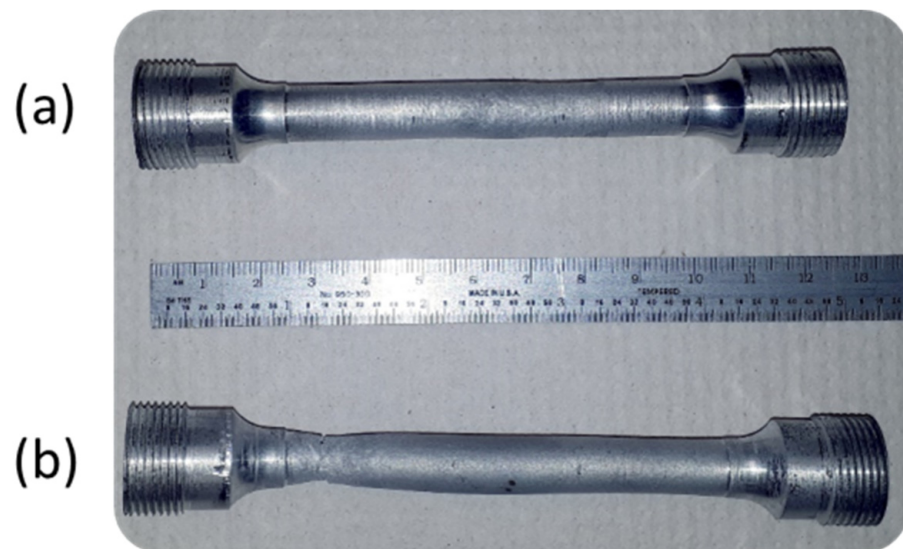


Figure 11. Gleebly 3800 OP-TMF test pieces after being tested until failure with a mechanical strain amplitude of 0.5% and a temperature cycling between 60 and 300 °C. Aging condition (a) T7, and (b) T7S.

Despite the fact that the Z-set simulations predict a lower stretching for the T7 condition compared to the T7S condition, the difference in slope between the experiment and the simulation is disproportionate. This is explained by the fact that the constitutive law involved in the simulation does not include the viscoplastic components relevant to moderately high strain rates. Indeed, the LM&C EV EP constitutive law (elastoviscosity characterized by creep and elastoplasticity by LCF tests) does not take into account the viscoplasticity of the material as a function of temperature for strain rates between

$10^{-4} \text{ s}^{-1}$  to  $10^{-2} \text{ s}^{-1}$ . The deformation mechanism in this range of strain rates is the gliding of dislocations, while for very low strain rates (elastoviscous regime) the strain is more activated by the diffusion of vacancy defects.

The model obviously does not take into account all the elements of the Gleeble<sup>®</sup> assembly system. Nevertheless, it would have been realistic to obtain simulated slopes lower than those resulting from the displacement of the jaw.

Figure 12 shows the evolution of the total strain fields at the maximum tension time (Figure 12a,d) and at the maximum compression time (Figure 12b,e) for both aging conditions. The upper third of the specimen seems to remain in tension despite the cycles whereas it is rather the lower zone (middle of the specimen) which works both in tension and compression. This is very marked for the T7S condition.

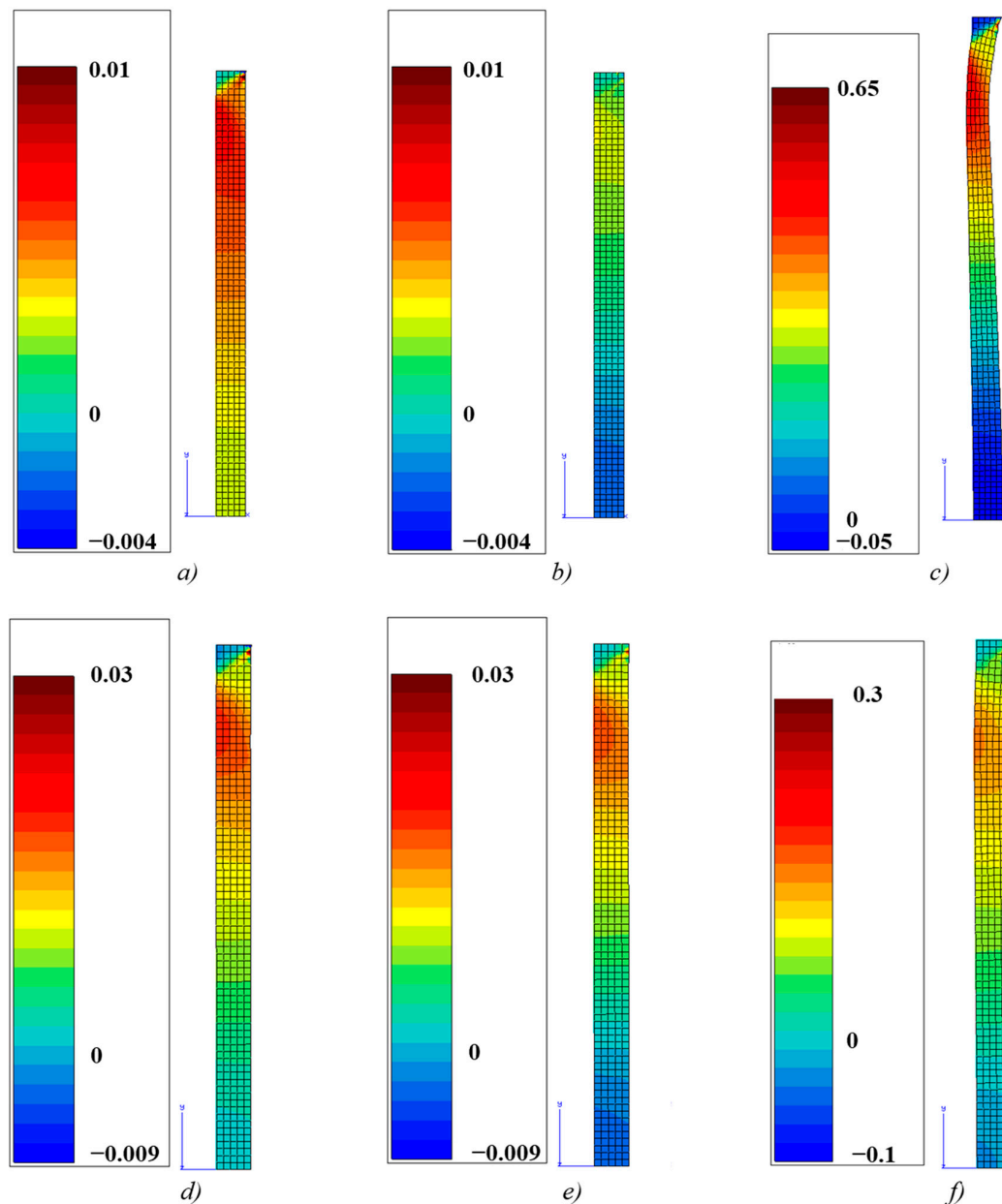


**Figure 12.** Total strain field on vertical axis for conditions T7 EV EP at (a) 250 s (tensile), (b) 300 s (compression) and (c) 19,700 s (cycle 197), and T7S EV EP at (d) 250 s (tensile), (e) 300 s (compression) and (f) 2300 s (cycle 23).

This behavior allows the specimen to generate a localized necking, over the cycles, on the upper third as the specimen lengthens. This is clearly visible in Figure 12c after 197 cycles for condition T7 and appears to be initiated in Figure 12f after 23 cycles for the T7S condition. It is this progressive stretching that is measured experimentally by the displacement of the movable jaw. This behavior is observed on the TMF specimens as shown in Figure 11b.

The general tendency of strain field distribution and its translation towards compression or tensile stages is the result of a competition between the cold tensile flow and the hot compressive flow. The results of this competition may change depending on aging condition. Because of the thermal gradients, stresses and strains distributions vary along the specimen, but also radially. The initial LM&C EV EP behavior law used for thermomechanical fatigue modelling has not been characterized for temperature-dependent viscoplasticity in a range of strain rates similar to those generated in LCF or TMF, so it did not take into account the viscoplastic behavior of the material for strain rates corresponding to those experimentally observed. An LM&C EV EP behavior law has been simulated with the elastoviscoplastic potential (Norton law with a non-zero yield strength) calibrated on LCF test cycles and it has shown that obtained displacement slopes were significantly reduced and it emphasized that it was possible to get closer to reality. This highlights the importance of mechanical characterization for large strain rates range. The obtained LM&C EV EP constitutive law makes it possible to reproduce rather objectively the evolutions of stresses in particular for the stabilized states but does not reconstitute the viscoplastic behavior of the material.

## 5. Conclusions

The aim of this work was to establish in a convincing manner whether or not the constitutive law of an aluminum alloy calibrated with creep tests and isothermal low-cycle fatigue tests performed at different temperatures but at one strain rate (CT + LCF) can model accurately the mechanical response during a TMF testing. From the modelling works performed in this study, the following conclusions were drawn:

The thermal gradient existing along the longitudinal axis of the TMF specimen has a significant impact on the mechanical response of the specimen. An accurate evaluation of the thermal profile is mandatory for accurate TMF modelling.

The CT + LCF calibration procedure was sufficient for the determination of a constitutive law providing an accurate prediction of the TMF hysteresis loops of an alloy having a stabilized microstructure.

The temperature gradient along the test piece was responsible for the gradual stretching of the specimen. This highlighted the importance of viscoplasticity and the need to characterize it carefully.

Although the CT + LCF procedure has predicted the gradual stretching of the specimen over the OP-TMF cycles, it was found that the viscoplasticity of the alloys must be characterized in the full range of strain rates considered in this type of loading for a better prediction.

The stretching was less significant in the T7 samples, because of the hardening effect of the metastable precipitated microstructure, as this was predicted by the simulation.

**Author Contributions:** Conceptualization, P.H. and D.L.; methodology, P.H., X.-G.C. and D.L.; software, P.H. and D.L.; validation, D.L., X.-G.C., R.M., D.M. and F.B.; writing—original draft preparation, P.H.; writing—review and editing, D.L., X.-G.C., R.M., D.M. and F.B.; supervision, D.L. and X.-G.C. All authors have read and agreed to the published version of the manuscript.

**Funding:** This research received no external funding.

**Institutional Review Board Statement:** Not applicable.

**Informed Consent Statement:** Informed consent was obtained from all subjects involved in the study.

**Data Availability Statement:** The raw/processed data required to reproduce these findings cannot be shared at this time due to technical or time limitations.

**Acknowledgments:** The authors would like to thank the Natural Sciences and Engineering Research Council of Canada (NSERC) and REGAL for financial support (NSERC Grant RDCPJ 468550–548 14) and also to Montupet and Rio Tinto Arvida teams for their collaboration. The authors wish to express their high appreciation of the work done by Dany Racine from UQAC for the conduction of TMF testing on the Gleeble. The authors are also grateful to Daniel Marcotte, Nathalie Moisan, Hervé Plancke and Marc Choquette for sharing their valuable knowledge and technical expertise.

**Conflicts of Interest:** The authors declare no conflict of interest.

## Appendix A. Comsol Simulation

### Appendix A.1. Generalities

The thermoelectric modelling of Joule heating was carried out on 1/8 of the geometry in order to limit the computation times by reduction of the mesh and by the use of three planes of symmetry as shown in Figure A1a. The cooling phases during a TMF cycle were performed by pulsed air flowing through the longitudinal hole of the specimen as detailed in Figure A1b. The jaws were continuously cooled by a water circuit at 20 °C to maintain their temperature during the heating phases (Figure A1c).

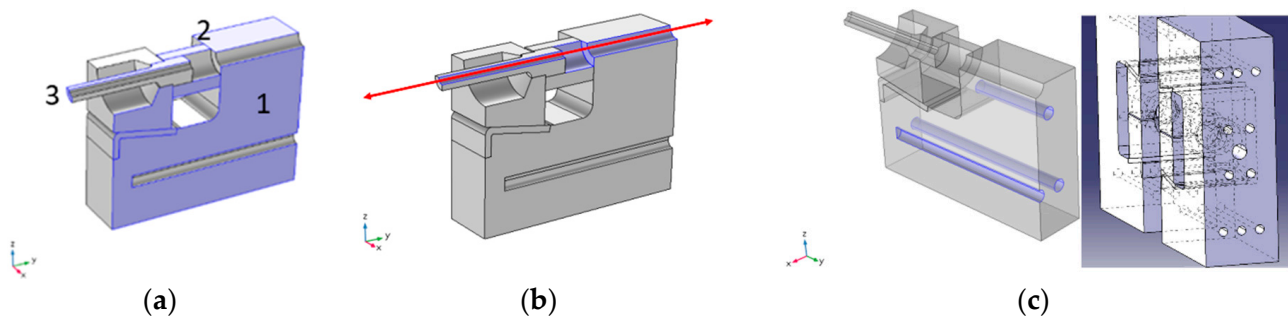


**Figure A1.** (a) The 3 planes of symmetry of the geometrical model, (b) Circulation of air for the cooling phases during the cycle, (c) Circuit of continuous water-cooling of the jaws at 20 °C in order to maintain its temperature.

The system was assumed quasi-incompressible to avoid all the numerical resolution complications due to the respective dilatation of the various elements of the assembly. Figure A2a shows the mesh chosen for modelling. The mesh sizes ranged between 1.2 mm and 5.7 mm. Figure A2b shows the contact interfaces implemented in the mechanical parameterization for the quasi-incompressible assembly with a contact pressure of  $10^7$  N/m<sup>2</sup>.

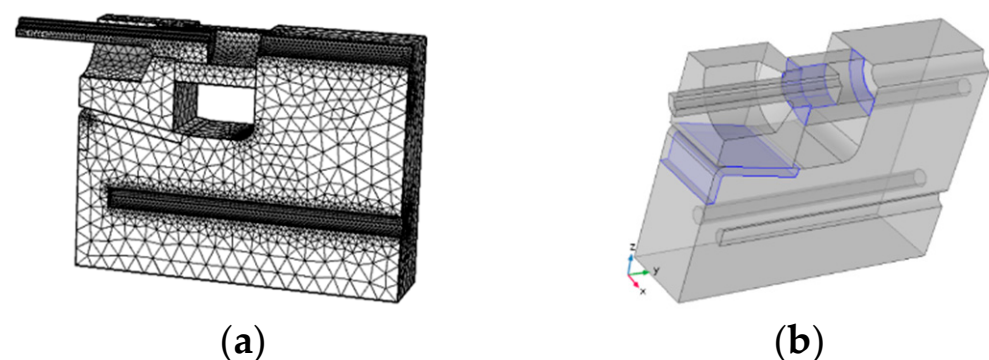


**Figure A2.** (a) Mesh of the system, (b) Mechanical parameterization for the quasi-incompressible assembly: pressure contact of  $10^7$  N/m<sup>2</sup>.

### Appendix A.2. Material Parameters

The thermophysical properties of AlSi7Cu3.5Mg0.15 (Mn, Zr, V) alloy were obtained by ThermoCalc [35] modelling with the TTAL7 [36] database and are based on the work of Larouche et al. [37] for the prediction of as-cast microstructure. A specific heat capacity of  $C_p = 1057 \text{ J}/(\text{kg}\cdot\text{K})$  was determined for this alloy. Figure A3 gives the evolutions of density, thermal and electrical conductivities as a function of the temperature.

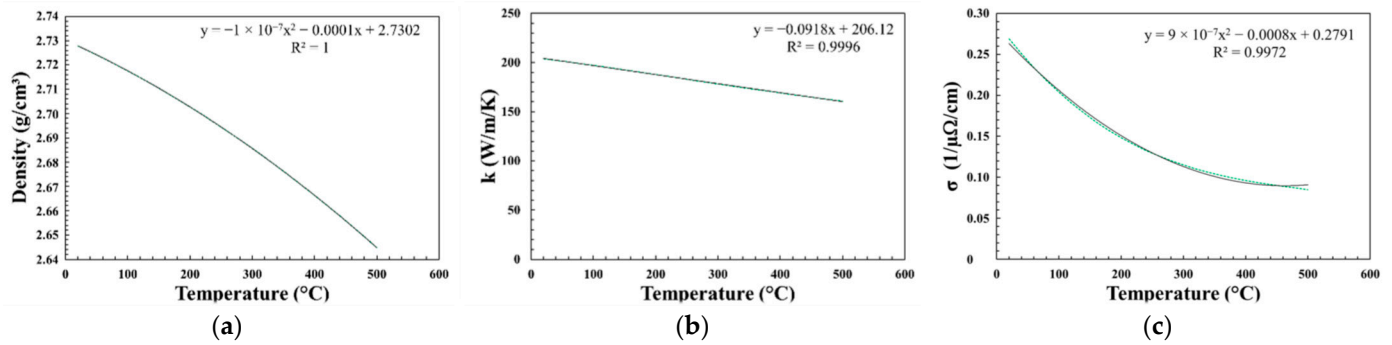


**Figure A3.** (a) Density, (b) thermal conductivity, (c) electrical conductivity of the AlSi7Cu3.5Mg0.15 (Mn, Zr, V) alloy as a function of temperature.

Table A1 shows the material data from the Comsol database adapted for the other elements of the assembly as well as the emissivity of the air for the radiation.

**Table A1.** Thermo-physical material parameters for other elements of the assembly.

Material	Density	k	$\sigma$	Cp	Emissivity
Copper clip	8960 kg/m <sup>3</sup>	400 W/m/K	$5.998 \times 10^7 \text{ S/m}$	385 J/kg/K	-
Steel jaws	7850 kg/m <sup>3</sup>	44.5 W/m/K	$4.032 \times 10^6 \text{ S/m}$	475 J/kg/K	-
Air	-	-	-	-	0.2

### Appendix A.3. Electrical Parameters

The input current is applied across the surface shown in Figure A4a and the electric ground has been placed on the surface of Figure A4b. The input current values were estimated based on the Power Angle data given by the Gleeble® system when a TMF test is performed. The plot of the experimental Power Angle (Figure A5a) was used as the input current trend setpoint signal and the associated input current values (Figure A5b) were calibrated to obtain the desired temperature in the middle of the test piece (maximum 300 °C) by trial-and-error simulation. The Power Angle is a raw data of the Gleeble® machine whose unit is not known.

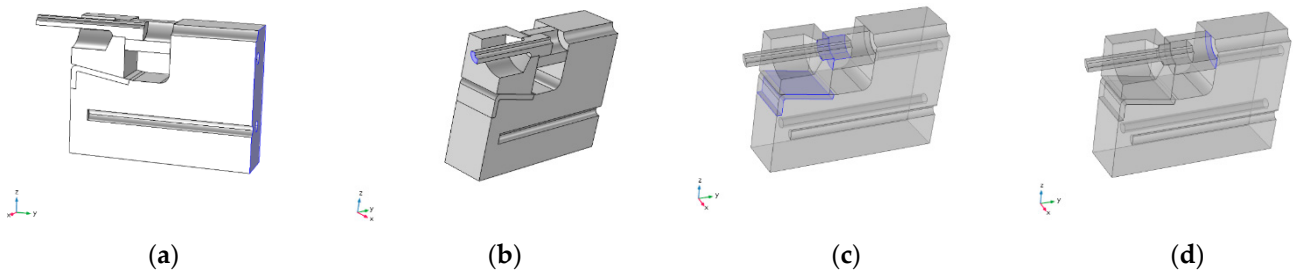


**Figure A4.** (a) Surfaces for current arrival, (b) Surfaces for mass, (c) "strong" electrical contact surfaces, (d) "weak" electrical contact surfaces.

With regard to the electrical contact at the interfaces, a constriction conductance was determined using the Cooper-Mikic-Yovanovich correlation (surface roughness of



an average height of the asperities of 1  $\mu\text{m}$  and average slope of 0.4 for a microhardness of 3 GPa) based on the previous contact pressure (Figure A4c) and secondly for a lower contact pressure of 100 kPa (Figure A4d). Indeed, the current has two possible paths [27] through the assembly, (1) primarily via the copper clip and the steel grip (Figure 1c) and, alternatively, (2) via the clamping steel nut (Figure A4d).

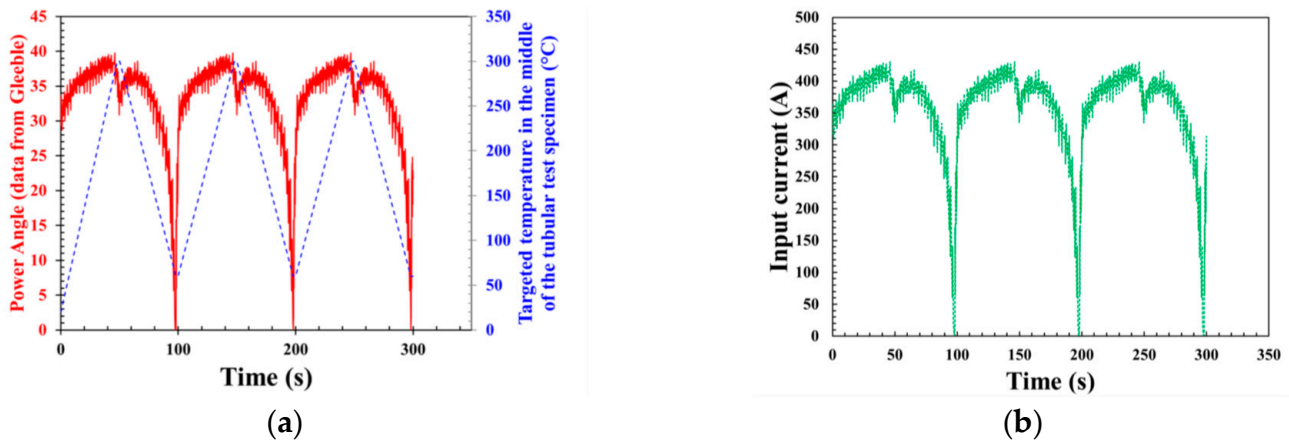


**Figure A5.** (a) Experimental power angle and targeted temperature in the middle of the specimen, (b) Input current applied in Comsol.

#### Appendix A.4. Thermal Parameters

The setting of the thermal problem data was essentially based on the establishment of the heat transfer coefficients of convective heat flux on the specific faces of the various components of the geometric model. Table A2 gives the chosen values for the different outer surfaces of the elements. Figure A6 describes the various surfaces and thermal assumptions for the model. For air-cooled interior surfaces during the TMF cycle cooling phases, Figure A7a shows the evolution of the heat transfer coefficient of convective heat flux on the inner surfaces of the nut and the jaw, this increases from 50 to 250  $\text{W}/(\text{m}^2 \cdot \text{K})$  respectively during the heating and cooling phases. For the internal surfaces of the specimen, Figure A7b shows the evolution of the heat transfer coefficient of the applied convective heat flux which has been calibrated by trial and error in order to obtain a triangular temperature variation between 60  $^{\circ}\text{C}$  and 300  $^{\circ}\text{C}$  in the middle of the test tube. Its specific curvature during the cooling phases is qualitatively based on the effect of the progressive air flow rate during these phases. The radiation of the surfaces of Figure A6f was applied according to the emissivity of the air given in the previous section. The thermal contact for the contact interfaces shown in Figure A6g was established by the equivalent resistive thin-film contact model with conductance of the layer of 0.00037  $\text{K} \cdot \text{m}^2/\text{W}$  [27].

**Table A2.** Convective heat flow applied to the surfaces of different elements.

Convective Heat Flow	Thermal Exchange Coefficient	Surface
External surface of the specimen	100 $\text{W}/(\text{m}^2 \cdot \text{K})$	Figure A6a
External surface of clamp and nut	50 $\text{W}/(\text{m}^2 \cdot \text{K})$	Figure A6b
External surface of copper clip	125 $\text{W}/(\text{m}^2 \cdot \text{K})$	Figure A6d

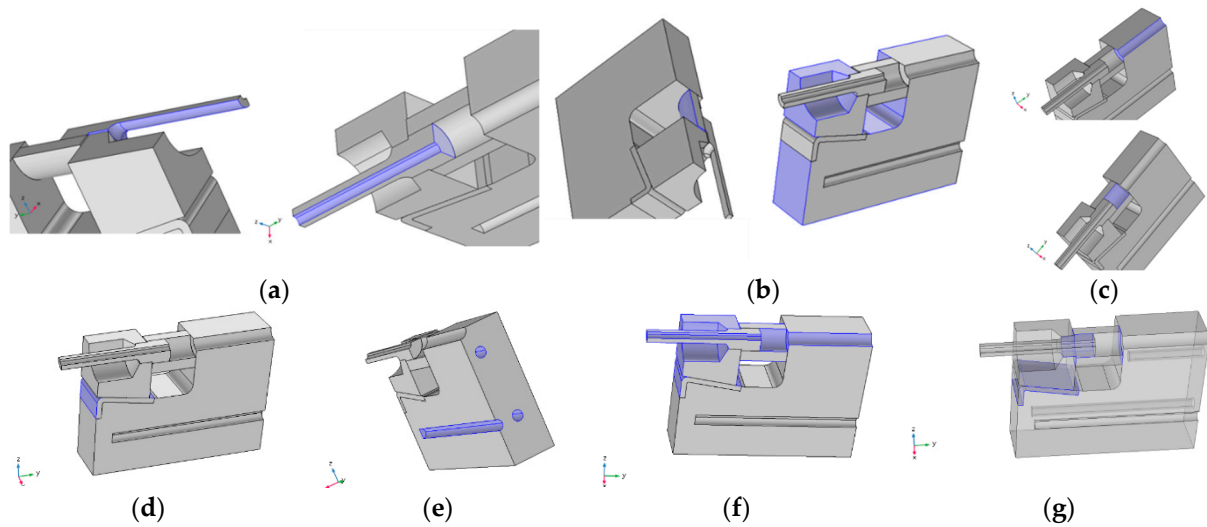


**Figure A6.** Convective heat flow on (a) external specimen and internal air-cooled specimen, (b) external nut and jaw + external grip, (c) internal jaw and internal air-cooled nut, (d) external copper clip; (e) fixed 20 °C temperature as continuous water cooling; (f) radiant surfaces; (g) thermal contact at the interfaces.

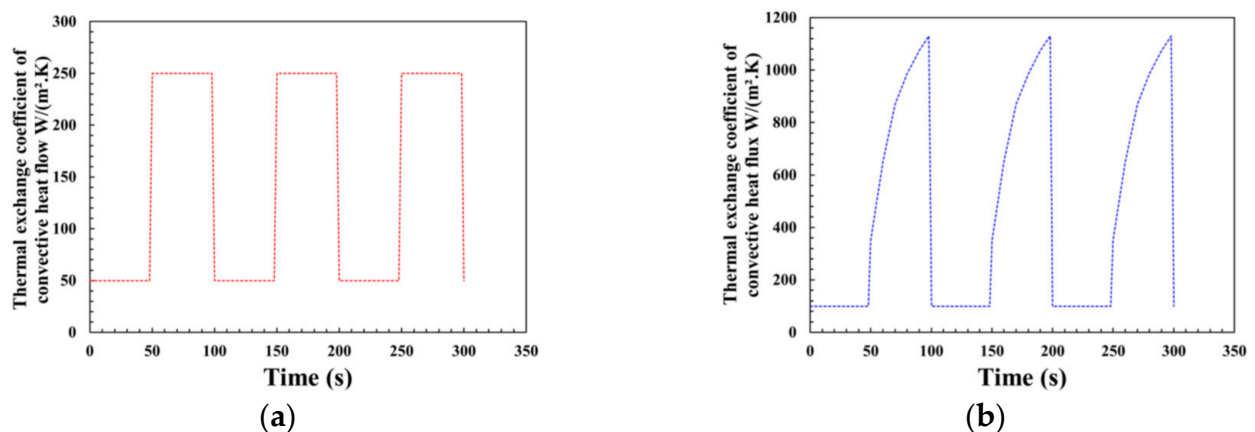


**Figure A7.** Evolution of thermal exchange coefficients of convective heat flow (a) nut and inner jaws, and (b) inner specimen during successive heating and cooling phases of TMF cycles.

## Appendix B. Z-Set Simulation

The mesh used for the thermomechanical Z-set modelling of the TMF test is presented in Figure A8. It is composed of 1286 square mesh nodes for 2D and axisymmetric representation of the tubular specimen as used and presented in Figure 4. The "top", "bottom", "ext" and "int" edges refer respectively to the jaw end, the middle of the specimen and the outer and inner surfaces. The Z-set digital simulation of the TMF test is performed in two stages. First of all, there is the thermal simulation according to the parameters obtained by the Comsol modeling of the Joule heating and then, the mechanical simulation, which used the results of the thermal simulation and the material behavior laws based on the LCF and creep testing.

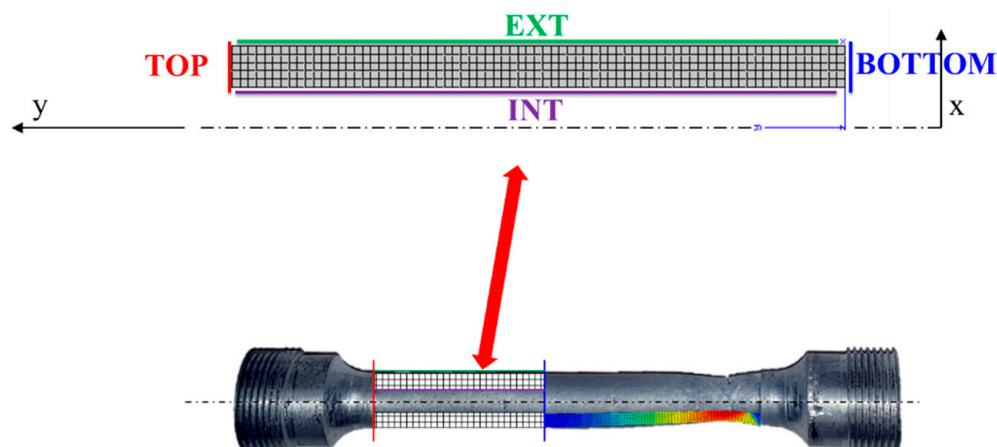


**Figure A8.** Z-set axisymmetric mesh of the TMF tubular specimen with the top edge: end of the jaw, and the bottom edge: as the middle of the specimen.

## References

- Huter, P.; Oberfrank, S.; Grün, F.; Stauder, B. Thermo-mechanical fatigue influence of copper and silicon on hypo-eutectic Al–Si–Cu and Al–Si–Mg cast alloys used in cylinder heads. *Int. J. Fatigue* **2016**, *88*, 142–155. [\[CrossRef\]](#)
- Huter, P.; Renhart, P.; Oberfrank, S.; Schwab, M.; Grün, F.; Stauder, B. High- and low-cycle fatigue influence of silicon, copper, strontium and iron on hypo-eutectic Al–Si–Cu and Al–Si–Mg cast alloys used in cylinder heads. *Int. J. Fatigue* **2016**, *82*, 588–601. [\[CrossRef\]](#)
- Firouzidor, V.; Rajabi, M.; Nejati, E.; Khomamizadeh, F. Effect of microstructural constituents on the thermal fatigue life of A319 aluminum alloy. *Mater. Sci. Eng. A* **2007**, *454–455*, 528–535. [\[CrossRef\]](#)
- Garat, M.; Laslaz, G. Improved Aluminium Alloys for Common Rail Diesel Cylinder Heads. *AFS Trans. Am. Foundry Soc.* **2007**, *21*, 1–8.
- Grieb, M.B.; Christ, H.J.; Plege, B. Thermomechanical fatigue of cast aluminium alloys for cylinder head applications—Experimental characterization and life prediction. *Procedia Eng.* **2010**, *2*, 1767–1776. [\[CrossRef\]](#)
- Tabibian, S.; Charkaluk, E.; Constantinescu, A.; Szymtka, F.; Oudin, A. TMF-LCF life assessment of a Lost Foam Casting 319 aluminum alloy. *Int. J. Fatigue* **2013**, *53*, 75–81. [\[CrossRef\]](#)
- Qin, J.; Racine, D.; Liu, K.; Chen, X.-G. Strain-controlled thermo-mechanical fatigue testing of aluminum alloys using the Gleeble® 3800 system. In Proceedings of the 16th International Conference on Aluminum Alloys ICAA16, Montreal, QC, Canada, 17 June 2018.
- Smith, T.J.; Maier, H.J.; Sehitoglu, H.; Fleury, E.; Allison, J. Modeling High-Temperature Stress-Strain Behavior of Cast Aluminum Alloys. *Metall. Mater. Trans. A* **1999**, *30A*, 133–146. [\[CrossRef\]](#)
- Toyoda, M.; Toda, H.; Ikuno, H.; Kobayashi, T.; Kobayashi, M.; Matsuda, K. Preferential orientation of precipitates during thermomechanical cyclic loading in an aluminum alloy. *Scr. Mater.* **2007**, *56*, 377–380. [\[CrossRef\]](#)
- Zhu, A.W.; Starke, E.A. Stress aging of Al-xCu alloys: Experiments. *Acta Mater.* **2001**, *49*, 2285–2295. [\[CrossRef\]](#)
- Lin, Y.C.; Xia, Y.-C.; Jiang, Y.-Q.; Zhou, H.-M.; Li, L.-T. Precipitation hardening of 2024-T3 aluminum alloy during creep aging. *Mater. Sci. Eng. A* **2013**, *565*, 420–429. [\[CrossRef\]](#)
- Beck, T.; Henne, I.; Löhe, D. Lifetime of cast AlSi6Cu4 under superimposed thermal-mechanical fatigue and high-cycle fatigue loading. *Mater. Sci. Eng. A* **2008**, *483*, 382–386. [\[CrossRef\]](#)
- Beck, T. Damage mechanism of cast Al–Si–Mg alloys under superimposed thermal-mechanical fatigue and high-cycle fatigue loading. *Mater. Sci. Eng. A* **2007**, *468*, 184–192. [\[CrossRef\]](#)
- Luft, J.; Beck, T.; Löhe, D. Thermal-Mechanical Fatigue Behaviour of the cast Aluminum alloy AlSi7Mg. In Proceedings of the 5th International Conference on Low Cycle Fatigue, Berlin, Germany, 9–11 September 2003; pp. 219–225.
- Azadi, M.; Shirazabad, M.M. Heat treatment effect on thermo-mechanical fatigue and low cycle fatigue behaviors of A356.0 aluminum alloy. *Mater. Des.* **2013**, *45*, 279–285. [\[CrossRef\]](#)
- Delprete, C.; Sesana, R.; Vercelli, A. Multiaxial damage assessment and life estimation: Application to an automotive exhaust manifold. *Procedia Eng.* **2010**, *2*, 725–734. [\[CrossRef\]](#)
- Toda, H.; Katano, J.; Kobayashi, T.; Akahori, T.; Niinomi, M. Assessment of Thermo-Mechanical Fatigue Behaviors of Cast Al-Si Alloys by Experiments and Multi-Step Numerical Simulation. *Mater. Trans.* **2005**, *46*, 111–117. [\[CrossRef\]](#)
- Merhy, E.; Rémy, L.; Maitournam, H.; Augustins, L. Crack growth characterisation of A356-T7 aluminum alloy under thermo-mechanical fatigue loading. *Eng. Fract. Mech.* **2013**, *110*, 99–112. [\[CrossRef\]](#)
- Tsuyoshi, T.; Sasaki, K. Low cycle thermal fatigue of aluminum alloy cylinder head in consideration of changing metrology microstructure. *Procedia Eng.* **2010**, *2*, 767–776. [\[CrossRef\]](#)

20. Wang, M.; Pang, J.C.; Zhang, M.X.; Liu, H.Q.; Li, S.X.; Zhang, Z.F. Thermo-mechanical fatigue behavior and life prediction of the Al-Si piston alloy. *Mater. Sci. Eng. A* **2018**, *715*, 62–72. [[CrossRef](#)]
21. Kliemt, C. Thermo-Mechanical Fatigue of Cast Aluminium Alloys for Engine Applications under Severe Conditions. Ph.D. Thesis, School of Engineering and Physical Sciences, Heriot-Watt University, Edimbourg, UK, 2012.
22. Bradaskja, B.; Koruza, J.; Fazarinc, M.; Knap, M.; Turk, R. A laboratory test for simulation of solidification on Gleeble 1500D thermo-mechanical simulator. *RMZ Mater. Geoenvironment* **2008**, *55*, 31–40.
23. Fabregue, D. Microstructure et Fissuration à Chaud lors du Soudage Laser d’alliages d’aluminium 6000. Ph.D. Thesis, Institut National Polytechnique de Grenoble, Grenoble, France, 2004.
24. Han, Q.; Hassan, M.I.; Viswanathan, S.; Saito, K. The Reheating-Cooling Method: A Technique for Measuring Mechanical Properties in the Nonequilibrium Mushy Zones of Alloys. *Metall. Mater. Trans. A* **2005**, *36A*, 2073–2080. [[CrossRef](#)]
25. Phillion, A.B.; Cockcroft, S.L.; Lee, P.D. A new methodology for measurement of semi-solid constitutive behavior and its application to examination of as-cast porosity and hot tearing in aluminum alloys. *Mater. Sci. Eng. A* **2008**, *491*, 237–247. [[CrossRef](#)]
26. Zhang, C.; Bellet, M.; Bobadilla, M.; Shen, H.; Liu, B. A Coupled Electrical-Thermal-Mechanical Modeling of Gleeble Tensile Tests for Ultra-High-Strength Steel at a High Temperature. *Metall. Mater. Trans. A* **2010**, *41*, 2304–2317. [[CrossRef](#)]
27. Palama Bongo, F. Caractérisation du Comportement Mécanique de l’alliage A356 à l’état Semi-Solide. Ph.D. Thesis, Université de Technologie de Compiègne, Compiègne, France, 2014.
28. Colley, L.J.; Wells, M.A.; Maijer, D.M. Tensile properties of as-cast aluminum alloy AA5182 close to the solidus temperature. *Mater. Sci. Eng. A* **2004**, *386*, 140–148. [[CrossRef](#)]
29. Martinez, R. *Modélisation Multi-échelles du Comportement d’un Alliage d’aluminium de Fonderie*; Institut de Chimie et des Matériaux Paris EST, Université Paris-Est Créteil: Paris, France, 2012.
30. Barlas, B. *Etude du Comportement et de l’endommagement en Fatigue d’alliages d’aluminium de Fonderie*; Sciences et Génie des Matériaux, Ecole Nationale Supérieure des Mines de Paris: Paris, France, 2004.
31. Lemaître, J.; Chaboche, J.L. *Mechanics of Solid Materials*; Cambridge University Press: Cambridge, UK, 1990.
32. Samuel, E.; Samuel, A.M.; Doty, H.W.; Valtierra, S.; Samuel, F.H. Intermetallic phases in Al-Si based cast alloys: New perspective. *Int. J. Cast Met. Res.* **2013**, *27*, 107–114. [[CrossRef](#)]
33. Heugue, P.; Larouche, D.; Breton, F.; Massinon, D.; Martinez, R.; Chen, X.-G. Precipitation Kinetics and Evaluation of the Interfacial Mobility of Precipitates in an AlSi7Cu3.5Mg0.15 Cast Alloy with Zr and V Additions. *Metals* **2017**, *9*, 777. [[CrossRef](#)]
34. Guillot, I.; Barlas, B.; Cailletaud, G.; Clavel, M.; Massinon, D. Thermomechanical fatigue and aging of cast aluminum alloy: A link between numerical modeling and microstructural approach. In *European Structural Integrity Society*; Rémy, L., Petit, J., Eds.; Elsevier: Amsterdam, The Netherlands, 2002; pp. 75–84.
35. Andersson, J.-O.; Helander, T.; Högglund, L.; Shi, P.; Sundman, B. Thermo-Calc & DICTRA, computational tools for materials science. *Calphad* **2022**, *26*, 273–312.
36. T. Ltd. (Ed.) *TTAL7, TT Al-Based Alloys Database*; Version 7.0; Surrey Technology Center: Guildford, UK, 2010.
37. Larouche, D. Computation of solidification paths in multiphase alloys with back-diffusion. *Calphad* **2007**, *31*, 490–504. [[CrossRef](#)]